Electronic supplementary information for

Molten salt electrolyte for electrochemical capacitor with energy density exceeding 50 W h/kg

Kuangyu Wang,[‡a] Ziyao Chen,[‡a] Kai Liu,[*b] Cheng Yang,[c] Haitian Zhang,[d] Yulong Wu,[a] Yuanzheng Long,[a] Hanlin Liu,[a] Yang Jin,[e] Meicheng Li,[b] Hui Wu[*a]

[a] State Key Lab of New Ceramics and Fine Processing, School of Materials Science and Engineering, Tsinghua University, Beijing 100084, P. R. China
[b] State Key Laboratory of Alternate Electrical Power System with Renewable Energy Sources, School of New Energy, North China Electric Power University, Beijing 102206, P. R. China
[c] Center for Advanced Mechanics and Materials Applied Mechanics Laboratory, Department of Engineering Mechanics, Tsinghua University, Beijing 100084, P. R. China
[d] Institute of Nuclear and New Energy Technology, Tsinghua University, Beijing 100084, P. R. China
[e] Research Center of Grid Energy Storage and Battery Application, School of Electrical Engineering, Zhengzhou University, Zhengzhou 450001, P. R. China

[*] Email: huiwu@tsinghua.edu.cn (H.W.); liukai21@ncepu.edu.cn (K.L.).

[‡] These authors contributed equally to this work.

1. Computational Details

(1) MD simulations

The empirical force field parameters for all ions were described by the OPLS-AA format and were taken from the previous work[1]. Other small molecules were first optimized at the B3LYP/def2tzvp level by Gaussian 16 software to obtain a reasonable structure. The force field parameters were referred to the Ligpargen website (http://zarbi.chem.yale.edu/ligpargen/)[2–4].

The modeling system of the bulk $AlCl_3$-NaCl-LiCl system consisted of 200 LiCl, 200 NaCl, and 600 $AlCl_3$ salt ions, leading to a simulation box with a dimension of 5.15*5.15*5.15 nm^3.

In the modeling system of the graphene slit pore, each pore wall was modeled as three sheets of graphene (5.15770*5.10480 nm) separated by a distance $\Delta = 0.3$ nm and fixed in space. The pore width H was defined as the minimum surface-to-surface distance between the two groups of graphene sheets in the z-direction. The carbon atoms in the graphene sheets were modeled as Lennard-Jones particles with $\sigma = 0.350$ nm and $\varepsilon = 0.334$ K J mol^{-1}. Moreover, the graphene sheets were kept fixed during all simulations.

In order to study the structure and ion dynamics of the nanoconfined $AlCl_3$-NaCl-LiCl, we initially included a suitable number of ions inside the slit pores. All the systems had a density of ~1.22 g cm^{-3}, which was similar to the bulk density of the molten salt at 398.15 K.

Atomistic simulations were performed using GROMACS 2020.6 package[5–7]. Packing Optimization for Molecular Dynamics Simulations (Packmol) program was used for building initial configurations of the bulk system for molecular dynamics simulations[8].

The simulation process was detailed as follows. The 5000-step steepest descent method and 5000-step conjugate gradient method were used to avoid unreasonable contact in the system. NPT ensemble was used to pre-equilibrate the system, and V-rescale

temperature coupling and Parrinello-Rahman pressure coupling were used to control the temperature to 398.15 K, and the pressure was maintained at 1 atm. The non-bonding cutoff radius was 1.2 nm, and the integration step was 2 fs. The bond length and angle were constrained by the LINCS algorithm. The two-way intercept was set to 1.2 nm, van der Waals interaction, and the long-distance electrostatic interaction was set by the particle-mesh Ewald method. The trajectory file during the simulation was saved every 10.0 ps.

(2) DFT simulations

All calculations were performed using the plane wave based periodic DFT method as implemented in the Vienna Ab Initio Simulation Package (VASP)[9,10]. The electron-ion interaction was described with the projector augmented wave (PAW) method[11,12]. The electron exchange and correlation energies were treated within the generalized gradient approximation in the Perdew-Burke-Ernzerhof functional (GGA-PBE)[13]. The plane wave basis was set up to 520 eV. Computations were satisfied until the energy and force converged within 10^{-6} eV and 0.02 eV $Å^{-1}$, respectively. A 6*8*1 supercell of 96 carbon atoms is constructed for the intercalation of $AlCl_4^-$.

To binding energy is calculated as following[14]:

$$E_{\text{binding}} = E_{[AlCl_4]_xC_n} - E_{C_n} - xE_{AlCl_4}$$

where $E_{[AlCl_4]_xC_n}$, E_{C_n}, and E_{AlCl_4} are the total energy of intercalated graphene, bulk graphene, and $AlCl_4$.

The intercalation potential is calculated as following[14]:

$$V = \frac{(\frac{3}{x}E_{[AlCl_4]_xC_n} + 4E_{[M+AlCl_4^-]} + E_{Al}) - (\frac{3}{x}E_{C_n} + 4E_{[M+Al_2Cl_7^-]})}{z}$$

where z is the number of electrons transferred per formula unit, x is the number of $AlCl_4$ molecules intercalated. E_{Al} is the total energy of a single Al atom in a bulk fcc structure.

$E_{[M^+ AlCl_4^-]}$ is the average of the total energy of $Li^+AlCl_4^-$ and $Na^+AlCl_4^-$, and $E_{[M^+ Al_2Cl_7^-]}$ is the average of the total energy of $Li^+Al_2Cl_7^-$ and $Na^+Al_2Cl_7^-$.

2. Supplementary Figures

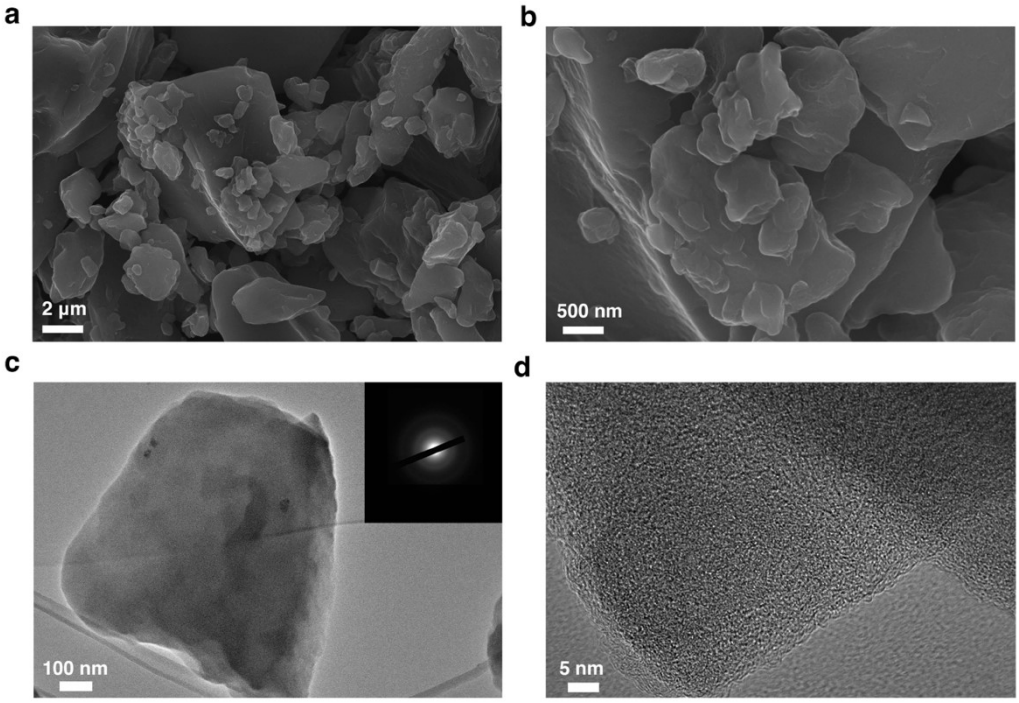

Fig. S1 (a), (b) SEM and (c), (d) TEM images of the AC powders.

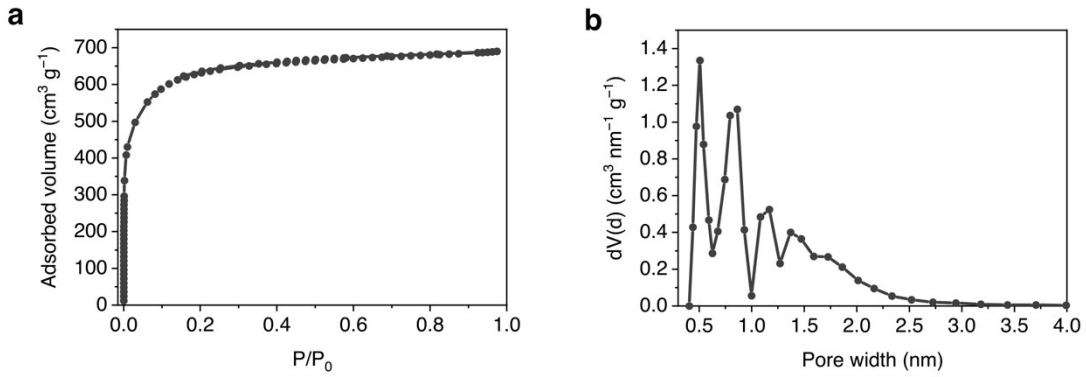

Fig. S2 (a) Argon adsorption-desorption isotherms and (b) pore size distributions of the AC powders.

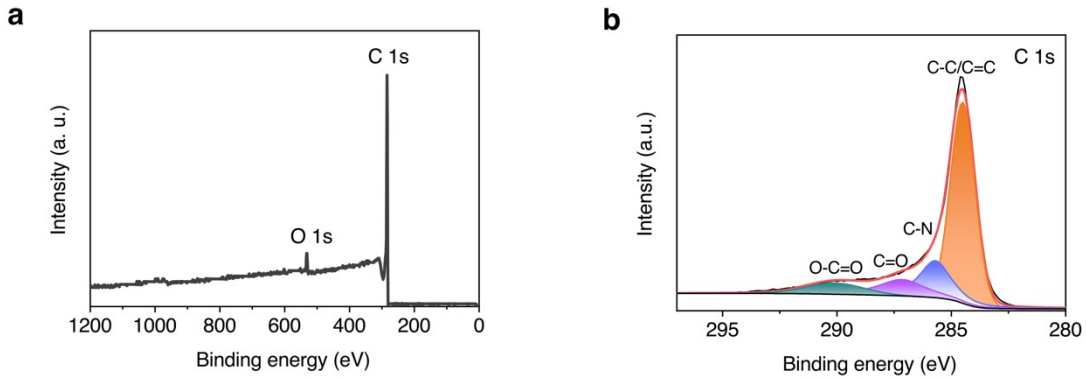

Fig. S3 XPS spectra of the AC powders.

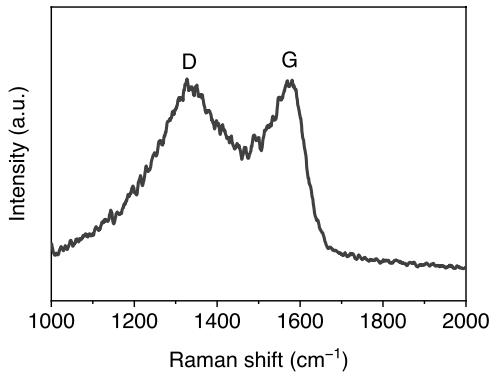

Fig. S4 Raman spectrum of the AC powders.

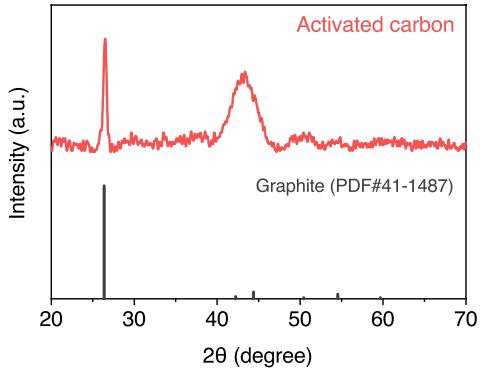

Fig. S5 XRD pattern of the AC powders.

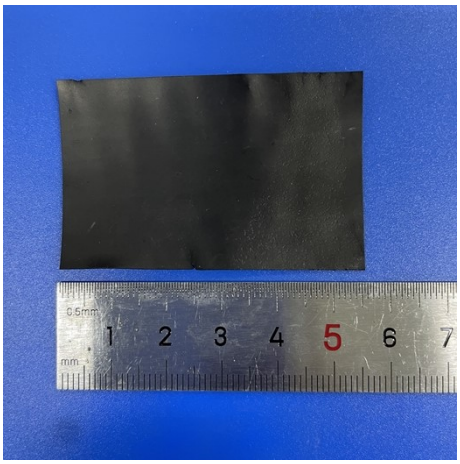

Fig. S6 Digital photo of the AC electrode.

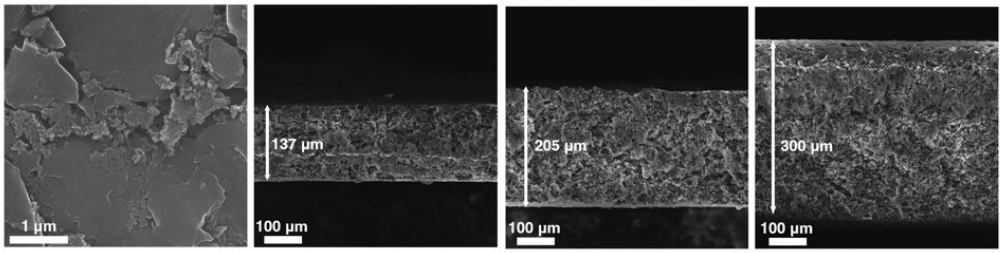

Fig. S7 SEM images of the surface and cross-sections of the AC electrodes with different thicknesses.

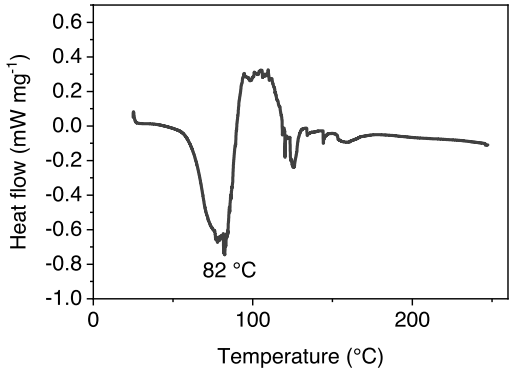

Fig. S8 DSC curve of the $AlCl_3$-NaCl-LiCl electrolyte.

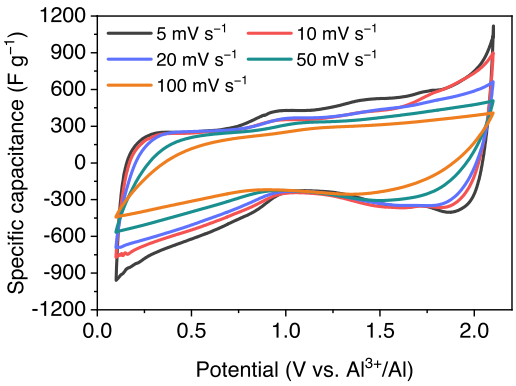

Fig. S9 CV curves of the AC electrode in the $AlCl_3$-NaCl-LiCl electrolyte at 125 °C and different scan rates.

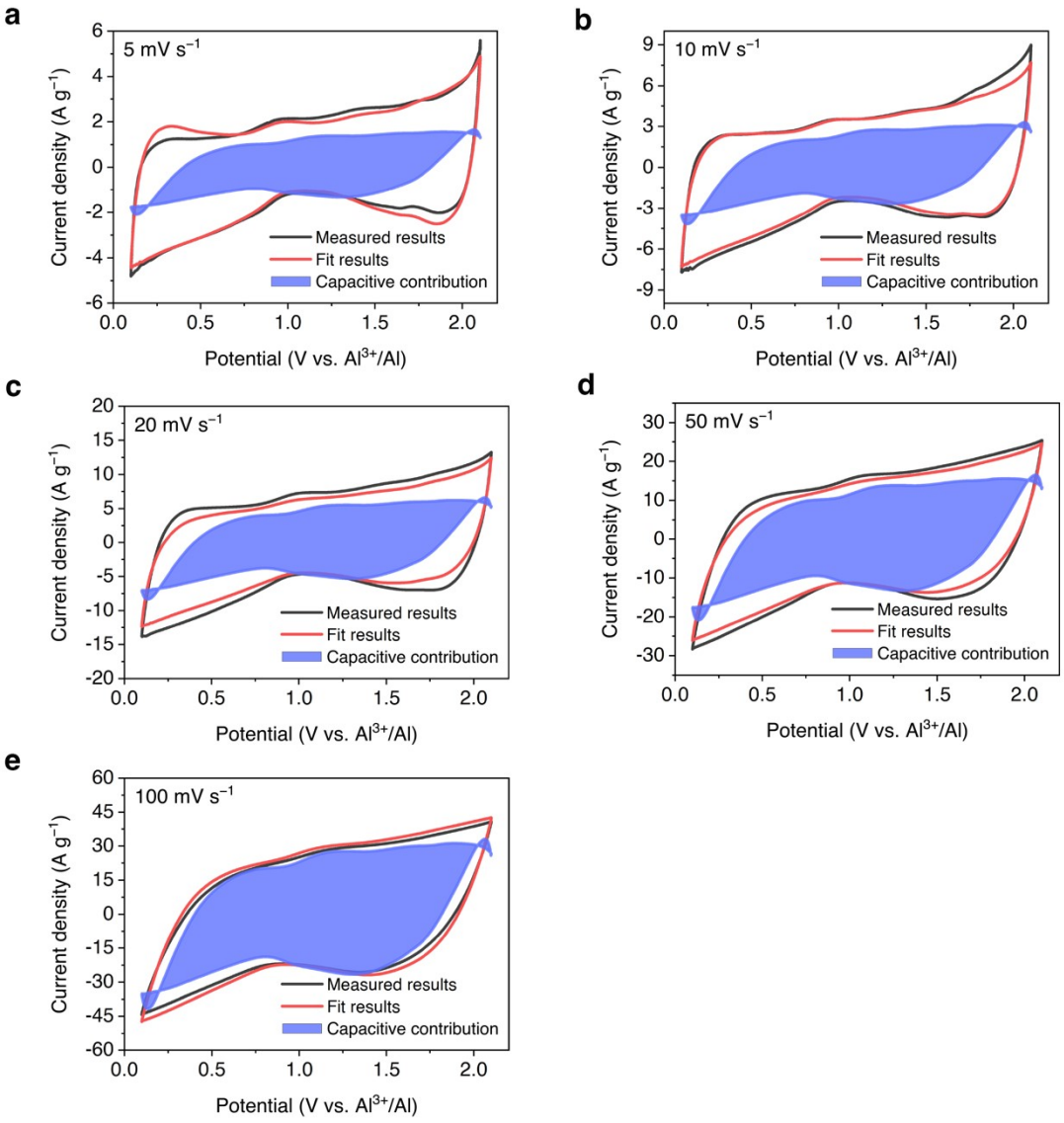

Fig. S10 CV curves of the AC electrode with experimental and fitted results at scan rates of (a) 5 mV s^{-1}, (b) 10 mV s^{-1}, (c) 20 mV s^{-1}, (d) 50 mV s^{-1}, and (e) 100 mV s^{-1}. The blue areas represented the capacitive contributions.

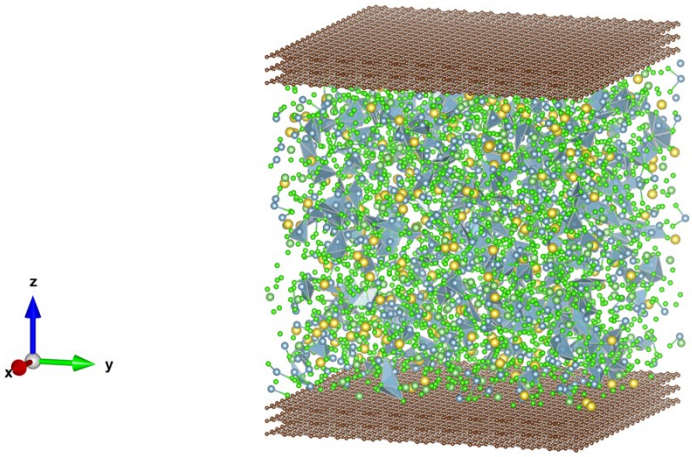

Fig. S11 Representative simulation snapshot of the $AlCl_3$-NaCl-LiCl system confined in the graphene slit pore with a width of 5.00 nm at 125 °C calculated by MD simulations.

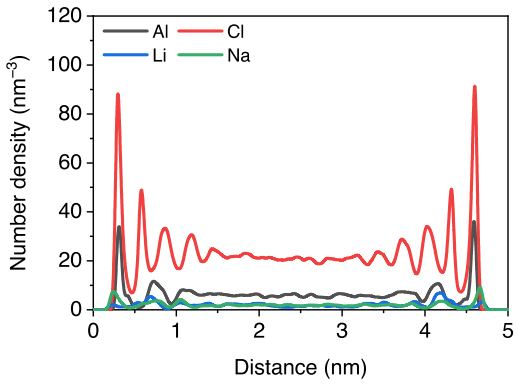

Fig. S12 Number density profiles along the z-direction of the ions of the $AlCl_3$-NaCl-LiCl system confined in the graphene slit pore with a width of 5.00 nm at 125 °C calculated by MD simulations.

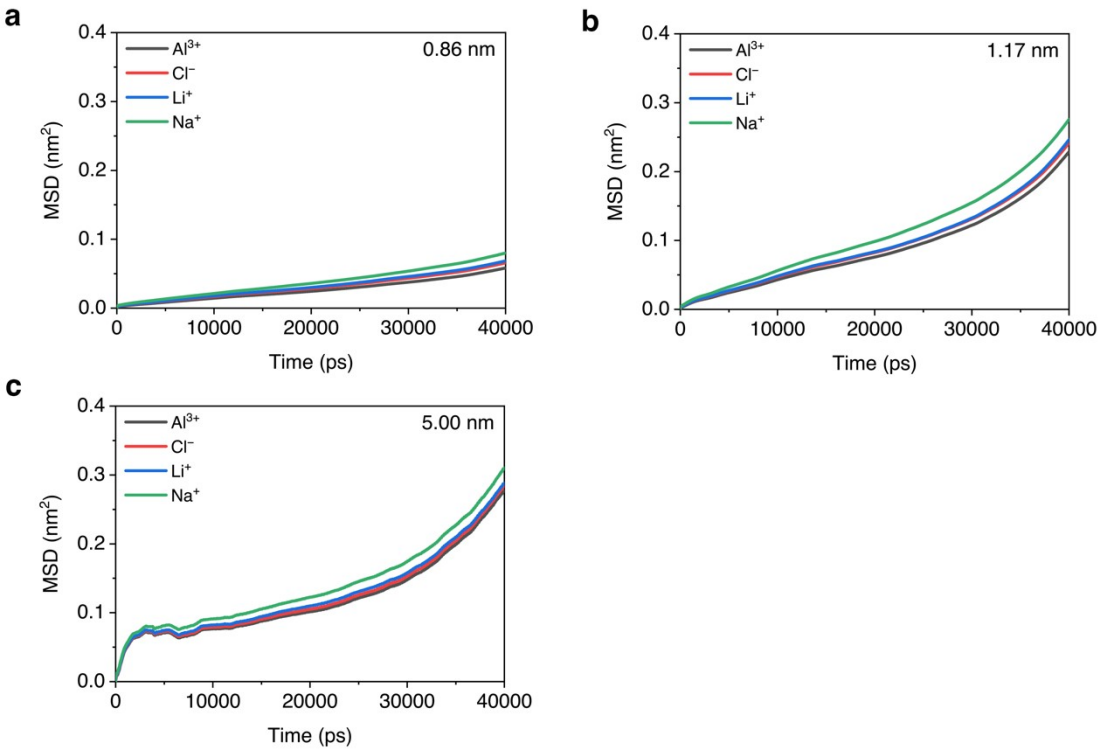

Fig. S13 MSDs of the ions of the $AlCl_3$-NaCl-LiCl system confined in graphene slit pores with widths of (a) 0.86 nm, (b) 1.17 nm, and (c) 5.00 nm at 125 °C calculated by MD simulations.

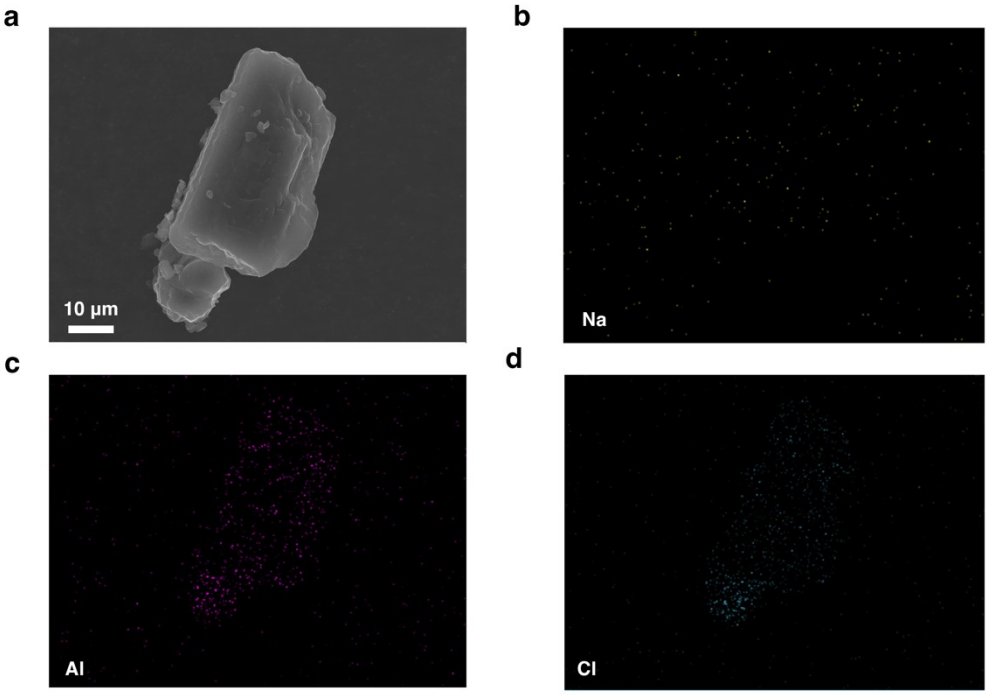

Fig. S14 (a) SEM image and corresponding EDX mappings of (b) Na, (c) Al, and (d) Cl of the MS@AC powders.

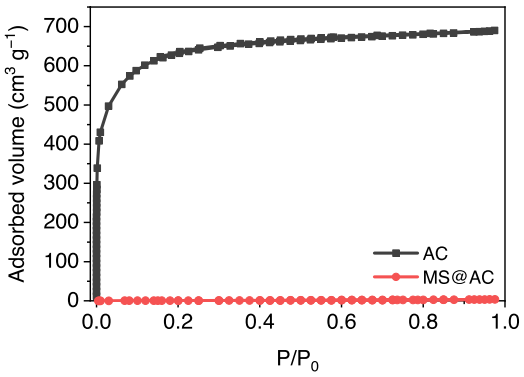

Fig. S15 Argon adsorption-desorption isotherms of the AC and MS@AC powders.

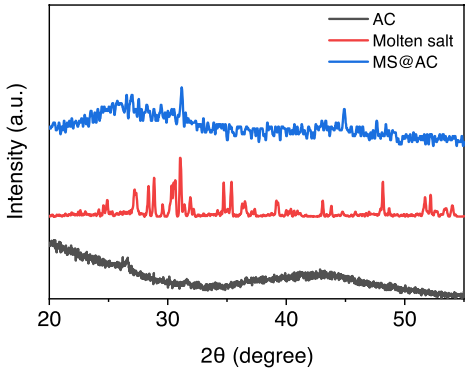

Fig. S16 XRD patterns of the AC, molten salt, and MS@AC powders.

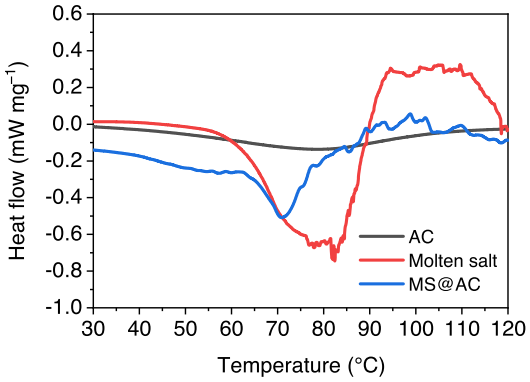

Fig. S17 DSC curves of the AC, molten salt, and MS@AC powders.

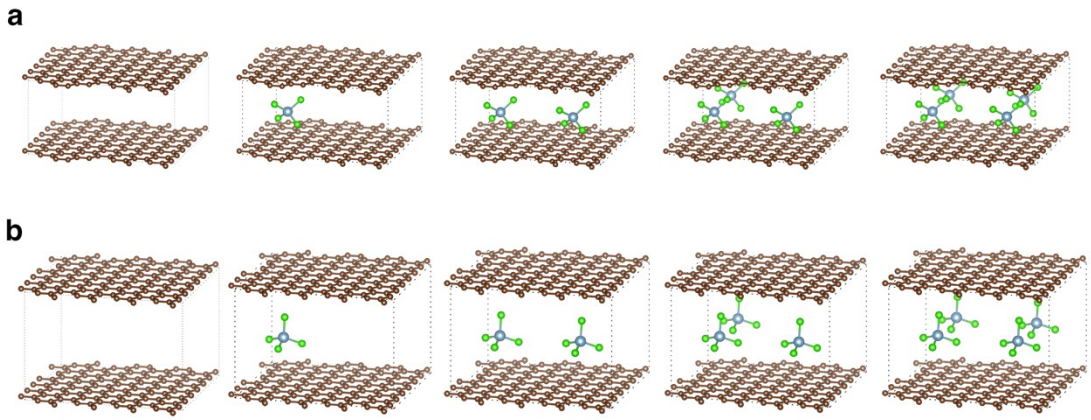

Fig. S18 Schematic representations of the optimized structures of the graphene slit pores with widths of (a) 0.86 nm and (b) 1.17 nm with 0, 1, 2, 3, 4 intercalated $AlCl_4$.

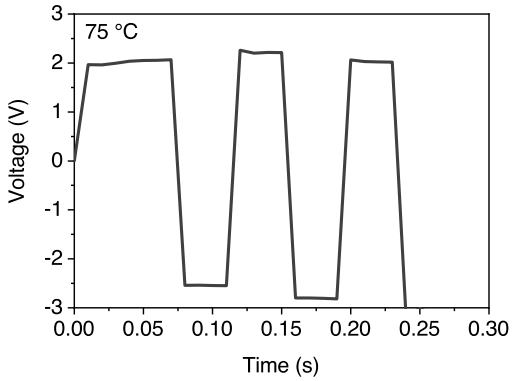

Fig. S19 GCD curve of the MS-EC cycled at 75 °C and a current density of 1 A g^{-1}.

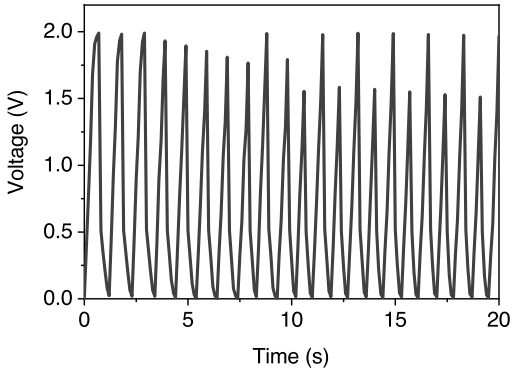

Fig. S20 Side reactions test. Two bare Mo meshes were applied as electrodes, and the device was cycled at 125 °C and a current density of 1 mA cm^{-1}.

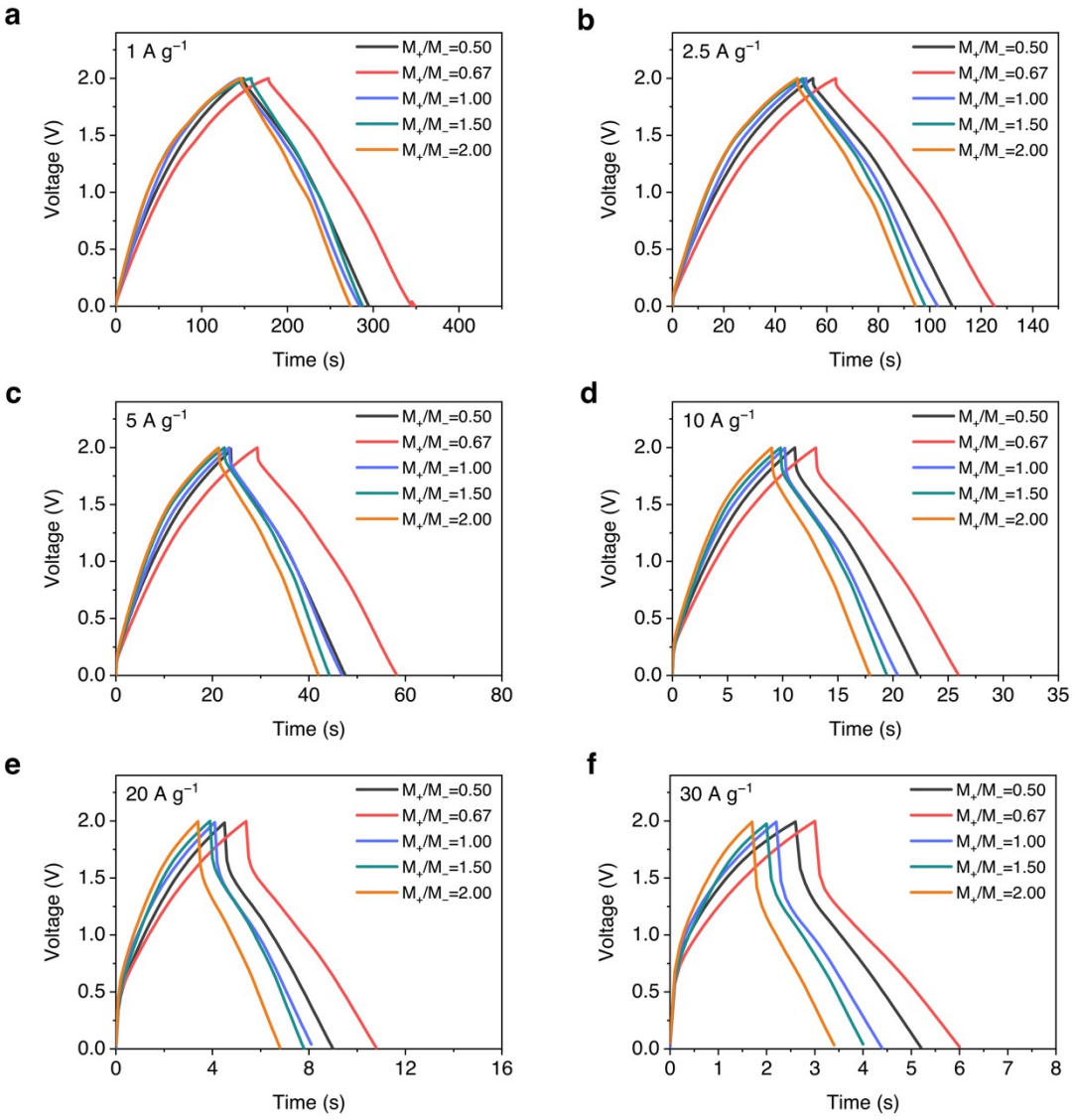

Fig. S21 GCD curves of MS-ECs with different M_+/M_- values at 125 °C and current densities of (a) 1 A g^{-1}, (b) 2.5 A g^{-1}, (c) 5 A g^{-1}, (d) 10 A g^{-1}, (e) 20 A g^{-1}, and (f) 30 A g^{-1}.

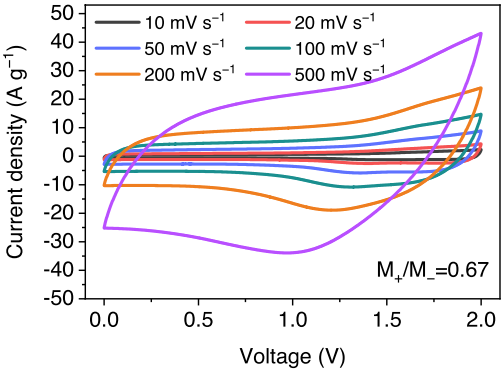

Fig. S22 CV curves of the MS-EC with an M_+/M_- value of 0.67 at 125 °C and different scan rates.

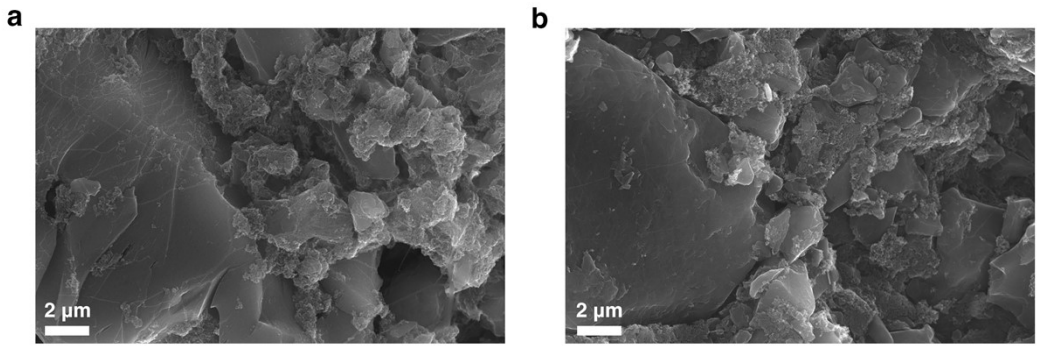

Fig. S23 SEM images of the electrodes (a) in the pristine state and (b) after cycling.

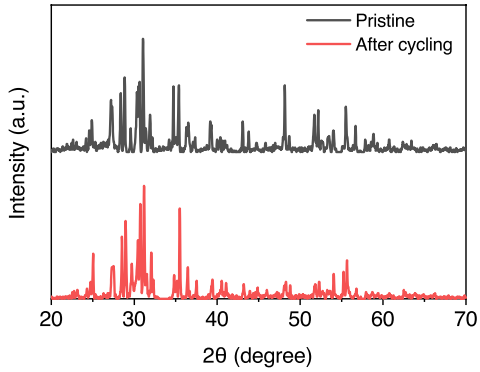

Fig. S24 XRD patterns of the $AlCl_3$-NaCl-LiCl electrolyte in the pristine state and after cycling.

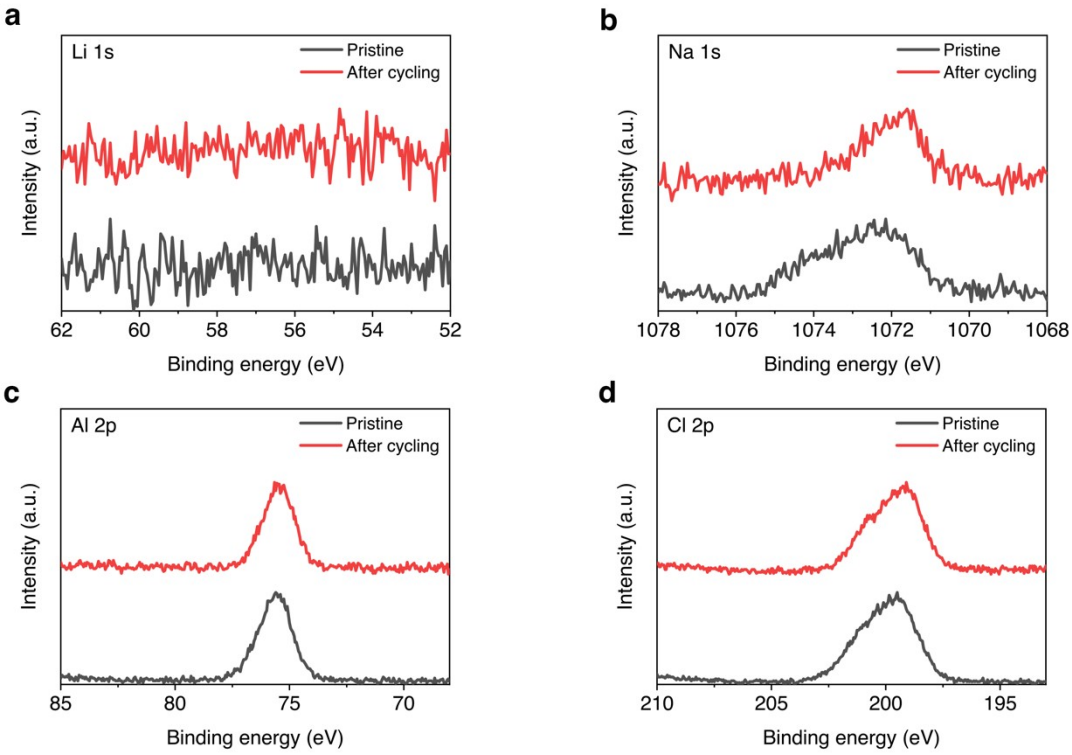

Fig. S25 XPS curves of (a) Li 1s, (b) Na 1s, (c) Al 2p, and (d) Cl 2p of the $AlCl_3$-NaCl-LiCl electrolyte in the pristine state and after cycling.

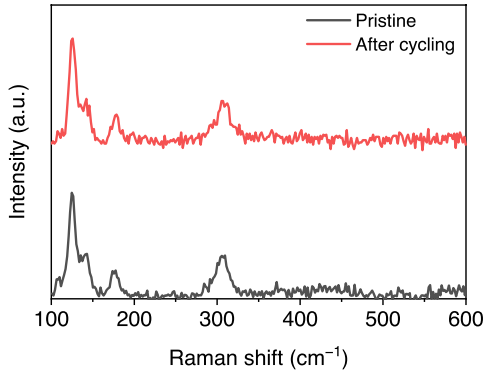

Fig. S26 Raman spectra of the $AlCl_3$-NaCl-LiCl electrolyte in the pristine state and after cycling.

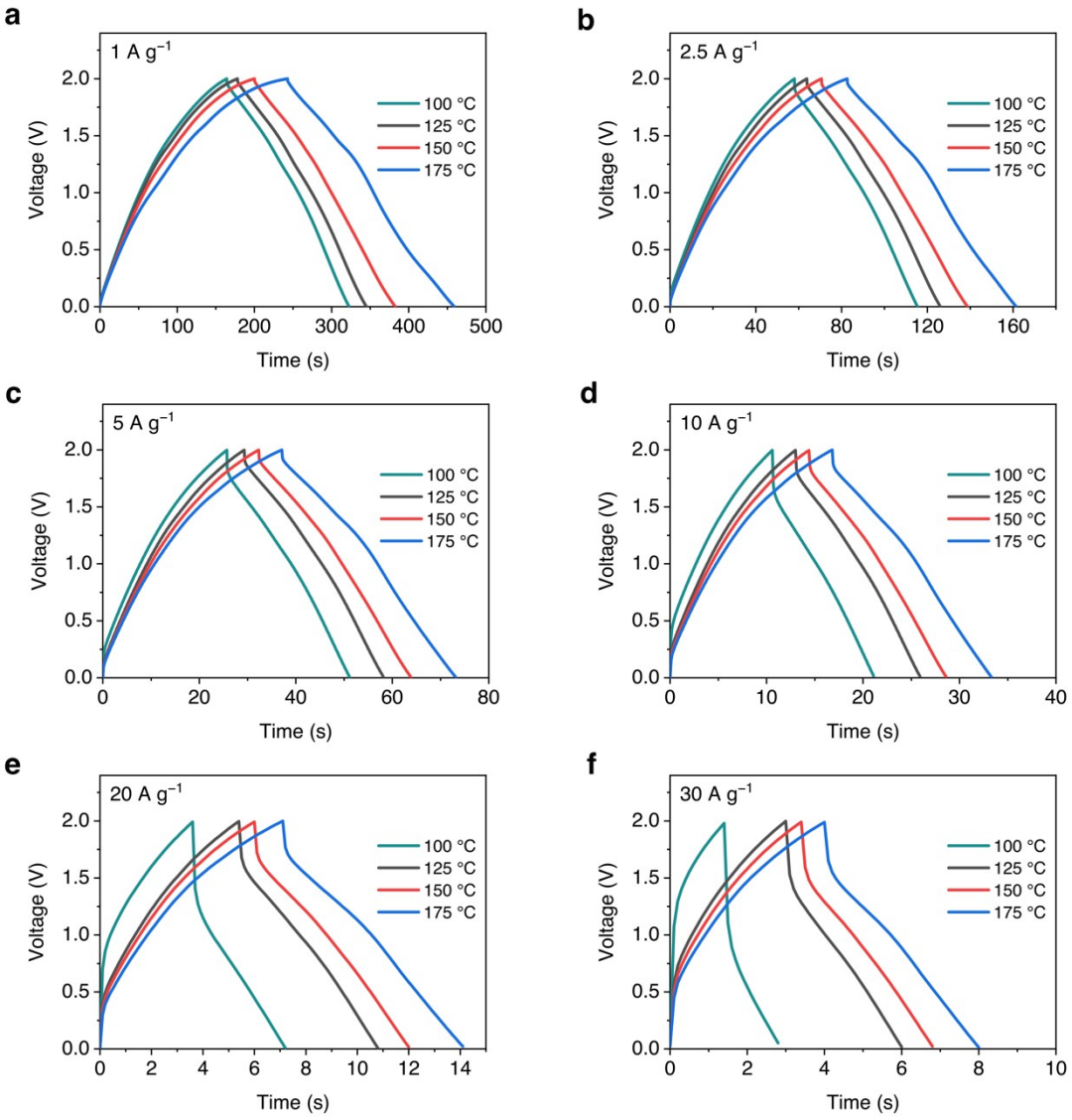

Fig. S27 GCD curves of the MS-EC cycled at different temperatures and current densities of (a) 1 A g^{-1}, (b) 2.5 A g^{-1}, (c) 5 A g^{-1}, (d) 10 A g^{-1}, (e) 20 A g^{-1}, and (f) 30 A g^{-1}.

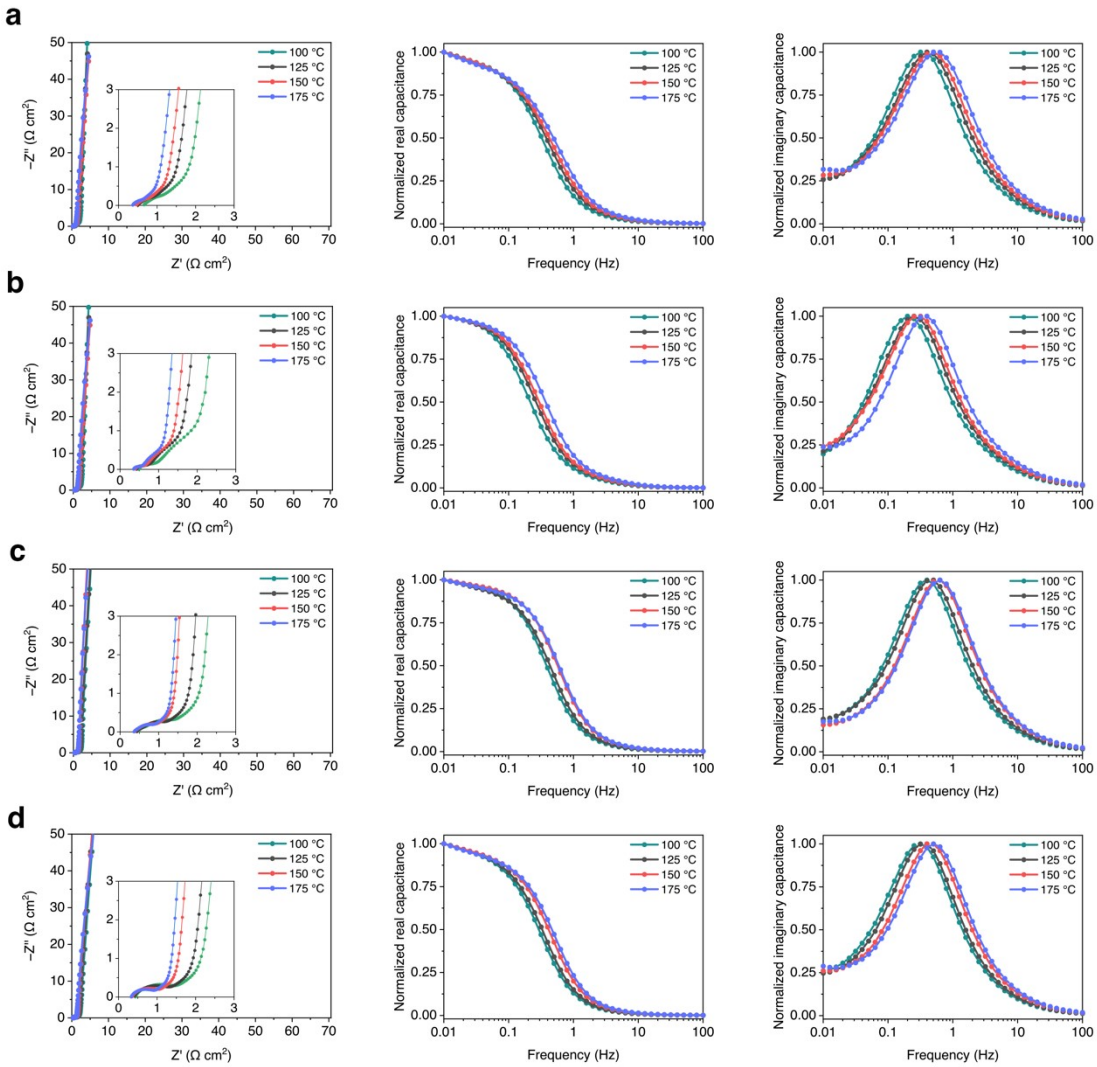

Fig. S28 EIS measurements of four MS-ECs at different temperatures. Nyquist plot, normalized real capacitance, and normalized imaginary capacitance of (a) Device #1, (b) Device #2, (c) Device #3, and (d) Device #4.

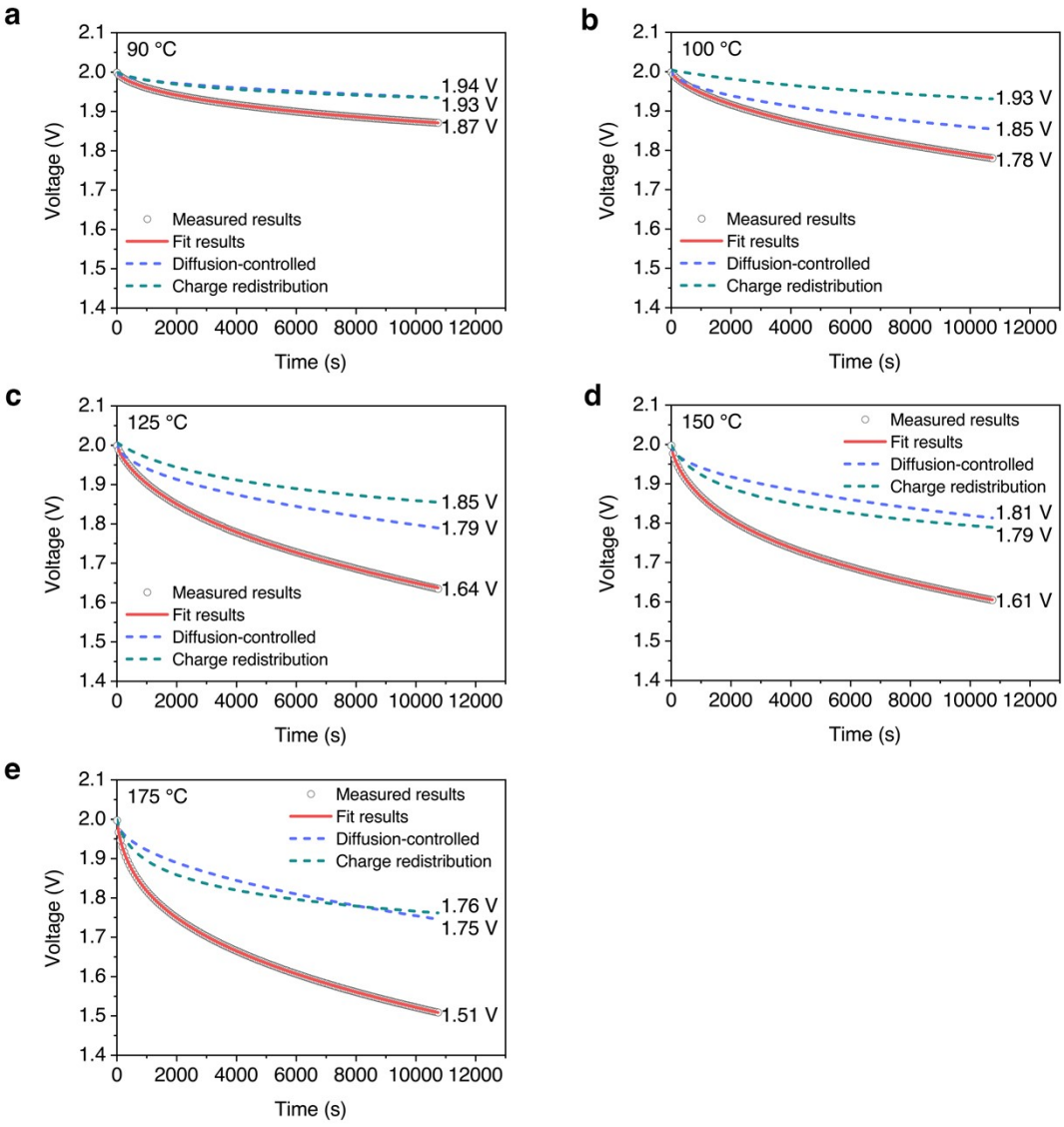

Fig. S29 Self-discharge profiles of the MS-EC at (a) 90 °C, (b) 100 °C, (c) 125 °C, (d) 150 °C, and (e) 175 °C with experimental and fitted results.

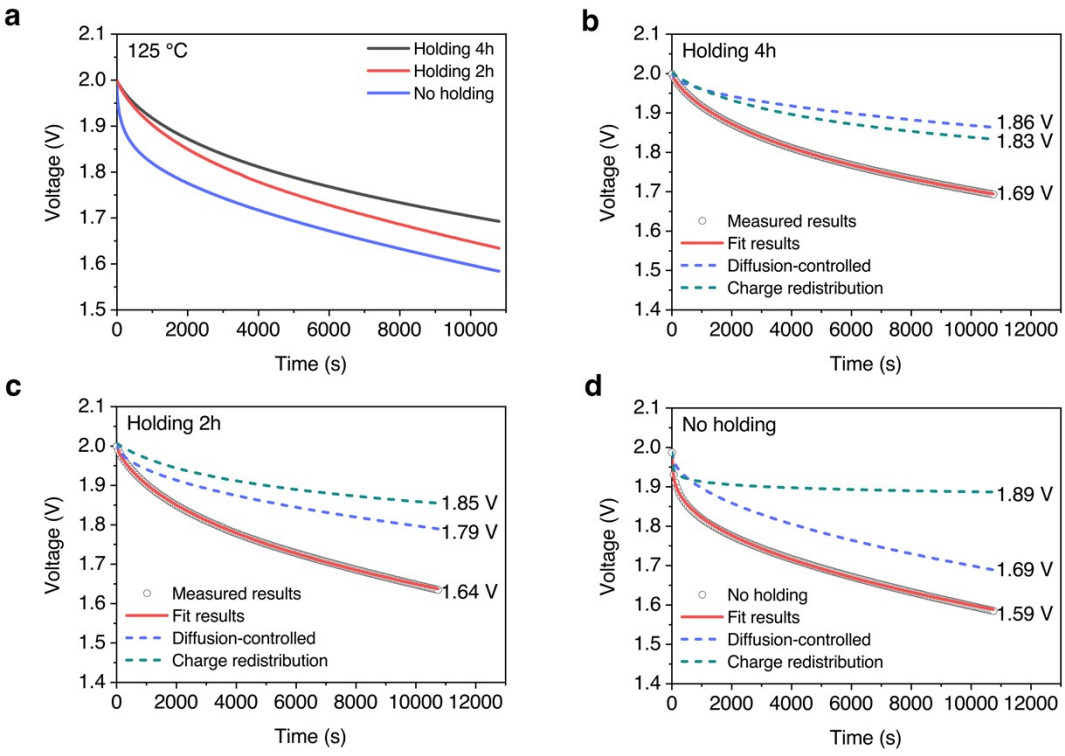

Fig. S30 (a) Self-discharge profiles of the MS-EC after different holding time and (b)-(d) the corresponding fitted results.

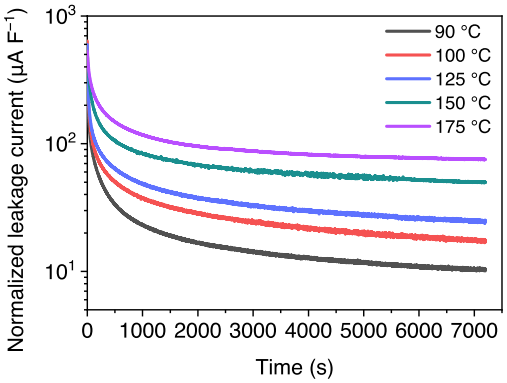

Fig. S31 Leakage current profiles of the MS-EC at different temperatures.

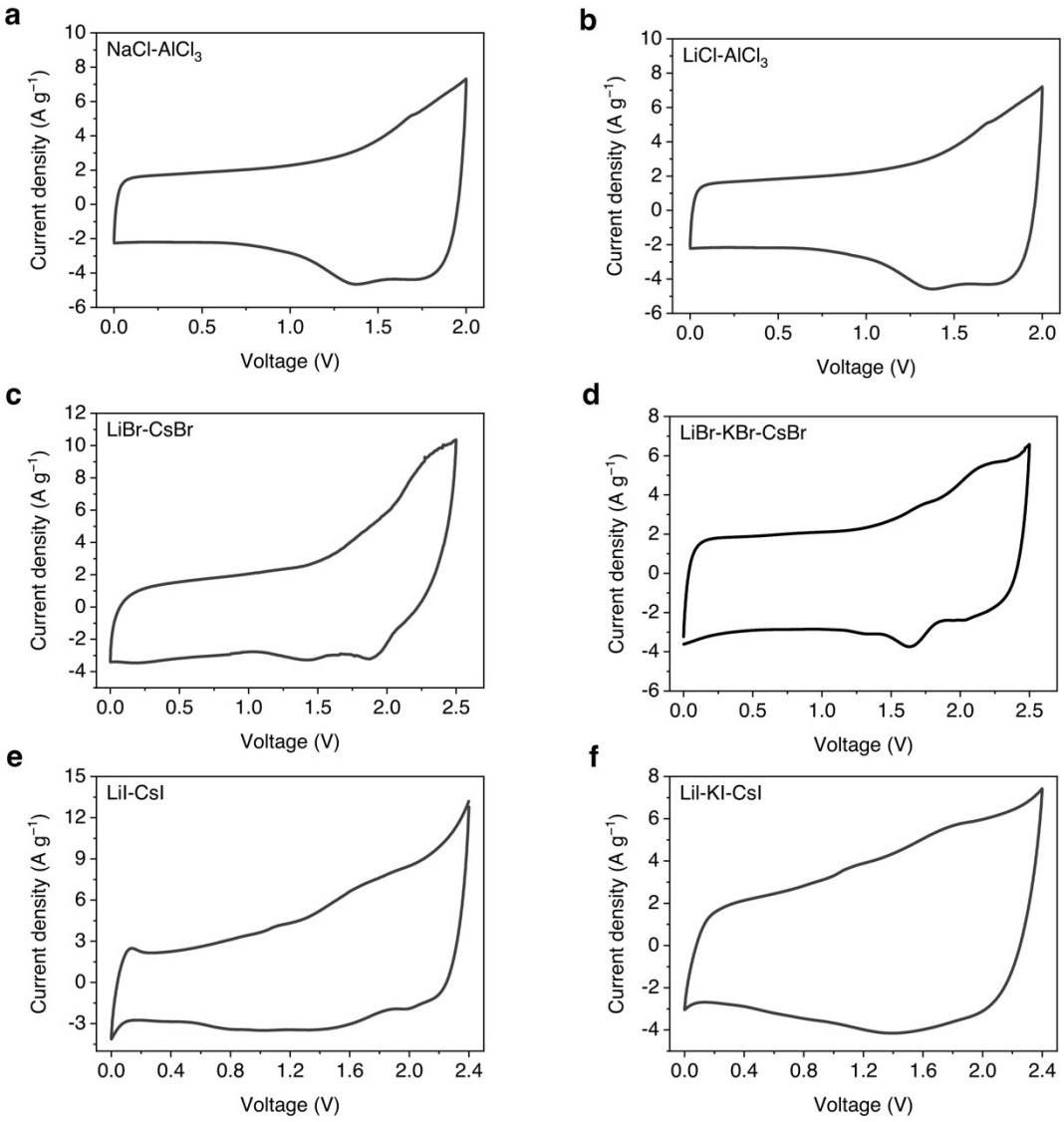

Fig. S32 CV curves of the MS-ECs with AC electrodes based on the (a) NaCl-$AlCl_3$, (b) LiCl-$AlCl_3$, (c) LiBr-CsBr, (d) LiBr-KBr-CsBr, (e) LiI-CsI, and (f) LiI-KI-CsI electrolytes at a scan rate of 20 mV s^{-1}.

3. Supplementary Tables

Table S1 Electrode thicknesses of the MS-ECs with different M_+/M_- values.

M_+/M_-	Cathode thickness (μm)	Anode thickness (μm)
0.50	~137	~300
0.67	~137	~205
1.00	~137	~137
1.50	~205	~137
2.00	~300	~137

Table S2 Element contents of the $AlCl_3$-NaCl-LiCl electrolyte in the pristine state and after cycling based on the ICP-OES analysis.

Element Content (wt%)	Li	Na	Al
Pristine	1.61	4.53	15.59
After cycling	1.75	4.74	15.96

[a)] Based on the results above, it can be calculated that the molar ratios of LiCl, NaCl, and $AlCl_3$ of the $AlCl_3$-NaCl-LiCl electrolyte in the pristine state and after cycling were 0.23:0.20:0.57 and 0.24:0.20:0.56, respectively.

Table S3 Performance metrics of the MS-ECs from the EIS measurements.

	Temperature (°C)	ESR (Ω cm^2)	R_{int} (Ω cm^2)	Peak Frequency (Hz)	Relaxation time constant (s)
Device #1	100	0.60	1.32	0.32	3.16
	125	0.46	1.10	0.40	2.51
	150	0.42	0.92	0.50	2.00
	175	0.33	0.75	0.50	2.00
Device #2	100	0.37	2.00	0.20	5.00
	125	0.34	1.50	0.25	4.00
	150	0.32	1.24	0.32	3.13
	175	0.30	1.05	0.40	2.50
Device #3	100	0.37	1.23	0.40	2.51
	125	0.36	1.08	0.50	2.00
	150	0.32	0.83	0.63	1.58
	175	0.32	0.78	0.63	1.58
Device #4	100	0.33	1.14	0.40	2.51
	125	0.29	1.03	0.40	2.51
	150	0.27	0.80	0.63	1.58
	175	0.27	0.73	0.63	1.58

Table S4 Consumed energy in the heating process of the MS-ECs.

	Stored energy (Wh kg^{-1})	Consumed energy (Wh kg^{-1})		
		Condition 1 [d]	Condition 2 [e]	Condition 3 [f]
Electrolyte [a]	134.0	2.1	11.2	21.5
Electrode [b]	50.0	1.9	4.9	14.6
Device [c]	36.4	2.0	9.5	19.6

[a] The heat capacity of the $AlCl_3$-NaCl-LiCl electrolyte is estimated to be 0.7 J g^{-1} K^{-1} according to reference[15]. The fusion enthalpy of the $AlCl_3$-NaCl-LiCl electrolyte is calculated to be 21.9 J g^{-1} from Fig. S8.

[b] The heat capacity of the AC electrode is estimated to be 0.7 J g^{-1} K^{-1} according to reference[16].

[c] The stored and consumed energy are calculated based on the masses of the electrolyte and the AC in the electrodes.

[d] In condition 1, the device is cooled down to 90 °C, where the electrolyte is in the liquid state, and then heated to 100 °C.

[f] In condition 2, the device is cooled down to 75 °C, where the electrolyte is in the solid state, and then heated to 100 °C.

[d] In condition 3, the device is cooled down to room temperature (25 °C) and then heated to 100 °C.

Table S5 Comparisons of the EC systems with AC electrodes based on the $AlCl_3$-NaCl-LiCl molten salt electrolyte and other electrolytes.

	Energy density (electrode) (Wh kg^{-1}) [e]	Energy density (electrolyte) (Wh kg^{-1}) [f]	Ionic conductivity (mS cm^{-1})	Price ($ kWh^{-1}) [g]	Safety hazard
Aqueous [a]	7–15	15–80	500–800	1–4	Corrosiveness
Organic [b]	20–25	10–20	5–50	100–300	Flammability, volatility, toxicity
Ionic liquid [c]	25–35	40–80	1–20	1000–3000	/
Molten salt [d]	35–50	107	100–300	28	High temperature

[a] The parameters of the ECs with aqueous electrolytes are calculated based on references[17–20].

[b] The parameters of the ECs with organic electrolytes are calculated based on references[20–22].

[c] The parameters of the ECs with ionic liquid electrolytes are calculated based on references[21–24].

[d] The parameters of the ECs with molten salt are calculated based on the experimental results of the MS-ECs with the $AlCl_3$-NaCl-LiCl electrolyte.

[e] The energy densities based on the active material mass in the electrodes correspond to the data with power densities of ~ 1 kW kg^{-1}.

[f] The energy densities based on the electrolyte mass are calculated based on the following equation[21].

$$E_{\text{electrolyte}} = \frac{1}{2}\alpha n m_0 F U$$

where $E_{\text{electrolyte}}$ is the energy density of an EC calculated based on the electrolyte mass, α represents the fraction of total salt removed from the bulk electrolyte upon complete charging, n refers to the charge number of the adsorbed ion, m_0 is the initial salt molality

in the electrolyte, F is Faraday's constant, and U is the operative voltage. In approximation, α is assumed to be 1.0 for aqueous electrolytes and 0.5 for the organic and ionic liquid electrolytes according to reference[21]. For the $AlCl_3$-NaCl-LiCl electrolyte, the molar ratio of Na^+, Li^+, $AlCl_4^-$, and $Al_2Cl_7^-$ is estimated to be 1:1:1:1 according to reference[25].

[g] The prices of the raw materials are obtained from www.alibaba.com.

Table S6 Melting points and electrochemical windows of salt mixtures consisting of different anions.

Anions	Melting point (°C)	Electrochemical window	
		Cathodic limit	Anodic limit
Fluoride (F^-) [26–28]	~480–700	N/A	~5.0 V *vs.* Li^+/Li
Chloride (Cl^-) [29]	~265–350	N/A	~3.7 V *vs.* Li^+/Li
Bromine (Br^-) [28,30]	~220–300	N/A	~3.2 V *vs.* Li^+/Li
Iodine (I^-) [31–33]	~200–300	N/A	~2.5 V *vs.* Li^+/Li
Chloroaluminate ($AlCl_4^-$, $Al_2Cl_7^-$, etc.) [34]	~75–180	~0 V *vs.* Al^{3+}/Al	~2.2 V *vs.* Al^{3+}/Al
Hydroxide (OH^-) [35,36]	~150–200	~−2.3 V *vs.* Ag^+/Ag	~0.2 V *vs.* Ag^+/Ag
Nitrate (NO_3^-) [37–40]	~80–230	~2.2 V *vs.* Li^+/Li	~3.8 V *vs.* Li^+/Li
Carbonate (CO_3^{2-}) [41–43]	~490–710	~−2.0 V *vs.* Ag/Ag_2SO_4	~0.4 V *vs.* Ag/Ag_2SO_4

References

1 S. V. Sambasivarao and O. Acevedo, *J. Chem. Theory Comput.*, 2009, **5**, 1038–1050.

2 W. L. Jorgensen and J. Tirado-Rives, *Proc. Natl. Acad. Sci. U. S. A.*, 2005, **102**, 6665–6670.

3 L. S. Dodda, J. Z. Vilseck, J. Tirado-Rives and W. L. Jorgensen, *J. Phys. Chem. B*, 2017, **121**, 3864–3870.

4 L. S. Dodda, I. C. De Vaca, J. Tirado-Rives and W. L. Jorgensen, *Nucleic Acids Res.*, 2017, **45**, W331–W336.

5 J. Fu, X. Ji, J. Chen, L. Chen, X. Fan, D. Mu and C. Wang, *Angew. Chemie*, 2020, **132**, 22378–22385.

6 H. Yang, X. Chen, N. Yao, N. Piao, Z. Wang, K. He, H. M. Cheng and F. Li, *ACS Energy Lett.*, 2021, **6**, 1413–1421.

7 N. N. Rajput, J. Monk, R. Singh and F. R. Hung, *J. Phys. Chem. C*, 2012, **116**, 5169–5181.

8 L. Martínez, R. Andrade, E. G. Birgin and J. M. Martínez, *J. Comput. Chem.*, 2009, **30**, 2157–2164.

9 G. Kresse and J. Furthmüller, *Comput. Mater. Sci.*, 1996, **6**, 15–50.

10 G. Kresse and J. Furthmüller, *Phys. Rev. B - Condens. Matter Mater. Phys.*, 1996, **54**, 11169–11186.

11 P. E. Blöchl, *Phys. Rev. B*, 1994, **50**, 17953–17979.

12 D. Joubert, *Phys. Rev. B - Condens. Matter Mater. Phys.*, 1999, **59**, 1758–1775.

13 J. P. Perdew, K. Burke and M. Ernzerhof, *Phys. Rev. Lett.*, 1996, **77**, 3865–3868.

14 P. Bhauriyal, A. Mahata and B. Pathak, *Phys. Chem. Chem. Phys.*, 2017, **19**, 7980–7989.

15 C. Robelin, P. Chartrand and A. D. Pelton, *J. Chem. Thermodyn.*, 2004, **36**, 683–699.

16 N. Querejeta, S. García, N. Álvarez-Gutiérrez, F. Rubiera and C. Pevida, *J. CO_2 Util.*, 2019, **33**, 148–156.

17 X. Sun, X. Zhang, H. Zhang, D. Zhang and Y. Ma, *J. Solid State Electrochem.*,

2012, **16**, 2597–2603.

18 Z. Sun, M. Zheng, H. Hu, H. Dong, Y. Liang, Y. Xiao, B. Lei and Y. Liu, *Chem. Eng. J.*, 2018, **336**, 550–561.

19 Z. Qiu, Y. Wang, X. Bi, T. Zhou, J. Zhou, J. Zhao, Z. Miao, W. Yi, P. Fu and S. Zhuo, *J. Power Sources*, 2018, **376**, 82–90.

20 C. Zhong, Y. Deng, W. Hu, J. Qiao, L. Zhang and J. Zhang, *Chem. Soc. Rev.*, 2015, **44**, 7484–7539.

21 A. Brandt and A. Balducci, *J. Power Sources*, 2014, **250**, 343–351.

22 E. Mourad, L. Coustan, P. Lannelongue, D. Zigah, A. Mehdi, A. Vioux, S. A. Freunberger, F. Favier and O. Fontaine, *Nat. Mater.*, 2017, **16**, 446–454.

23 Q. D. Nguyen, J. Patra, C. Te Hsieh, J. Li, Q. F. Dong and J. K. Chang, *ChemSusChem*, 2019, **12**, 449–456.

24 F. Béguin, V. Presser, A. Balducci and E. Frackowiak, *Adv. Mater.*, 2014, **26**, 2219–2251.

25 A. A. Fannin, L. A. King and D. W. Seegmiller, *J. Electrochem. Soc.*, 1972, **119**, 801.

26 K. Lipkina, K. Palinka, E. Geiger, B. W. N. Fitzpatrick, O. S. Vălu, O. Beneš and M. H. A. Piro, *J. Nucl. Mater.*, 2022, **568**, 153901.

27 L. Xu, Y. Xiao, Q. Xu, A. Van Sandwijk, J. Li, Z. Zhao, Q. Song and Y. Yang, *RSC Adv.*, 2016, **6**, 84472–84479.

28 A. Abbasalizadeh, A. Malfliet, S. Seetharaman, J. Sietsma and Y. Yang, *J. Sustain. Metall.*, 2017, **3**, 627–637.

29 T. Murakami, T. Nohira, Y. H. Ogata and Y. Ito, *Electrochem. Solid-State Lett.*, 2005, **8**, 8–11.

30 T. Kasajima, T. Nishikiori, T. Nohira and Y. Ito, *J. Electrochem. Soc.*, 2004, **151**, 335–339.

31 Q. Gong, W. Ding, A. Bonk, H. Li, K. Wang, A. Jianu, A. Weisenburger, A. Bund and T. Bauer, *J. Power Sources*, 2020, **475**, 228674.

32 K. Kumamoto, A. Kishimoto and T. Uda, *J. Appl. Electrochem.*, 2020, **50**, 1209–1216.

33 H. Yu, H. Lu, X. Hu, J. Liu and Y. Cao, *Mater. Chem. Phys.*, 2020, **247**, 122865.

34 J. Tu, J. Wang, H. Zhu and S. Jiao, *J. Alloys Compd.*, 2020, **821**, 153285.

35 J. Yang, H. Muroyama, T. Matsui and K. Eguchi, *J. Power Sources*, 2014, **245**, 277–282.

36 M. H. Miles, *J. Appl. Electrochem.*, 2003, **33**, 1011–1016.

37 Y. Niu, Z. Wu and J. Du, *J. Electrochem. Soc.*, 2013, **160**, A1375–A1379.

38 M. Chen, Y. Shen, S. Zhu and P. Li, *Vacuum*, 2017, **145**, 225–233.

39 Z. Li and Z. G. Wu, *Sol. Energy Mater. Sol. Cells*, 2016, **155**, 341–347.

40 V. Giordani, D. Tozier, H. Tan, C. M. Burke, B. M. Gallant, J. Uddin, J. R. Greer, B. D. McCloskey, G. V. Chase and D. Addison, *J. Am. Chem. Soc.*, 2016, **138**, 2656–2663.

41 H. Yin, D. Tang, H. Zhu, Y. Zhang and D. Wang, *Electrochem. Commun.*, 2011, **13**, 1521–1524.

42 D. Tang, K. Zheng, H. Yin, X. Mao, D. R. Sadoway and D. Wang, *Electrochim. Acta*, 2018, **279**, 250–257.

43 T. Kojima, Y. Miyazaki, K. Nomura and K. Tanimoto, *J. Electrochem. Soc.*, 2008, **155**, F150.